nature nanotechnology

SUPPLEMENTARY INFORMATION

DOI: 10.1038/NNANO.2017.134

In the format provided by the authors and unedited.

Topical tissue nano-transfection mediates non-viral stroma reprogramming and rescue

Daniel Gallego-Perez, Durba Pal, Subhadip Ghatak, Veysi Malkoc, Natalia Higuita-Castro, Surya Gnyawali, Lingqian Chang, Wei-Ching Liao, Junfeng Shi, Mithun Sinha, Kanhaiya Singh, Erin Steen, Alec Sunyecz, Richard Stewart, Jordan Moore, Thomas Ziebro, Robert G. Northcutt, Michael Homsy, Paul Bertani, Wu Lu, Sashwati Roy, Savita Khanna, Cameron Rink, Vishnu B. Sundaresan, Jose J. Otero, L. James Lee, Chandan K. Sen

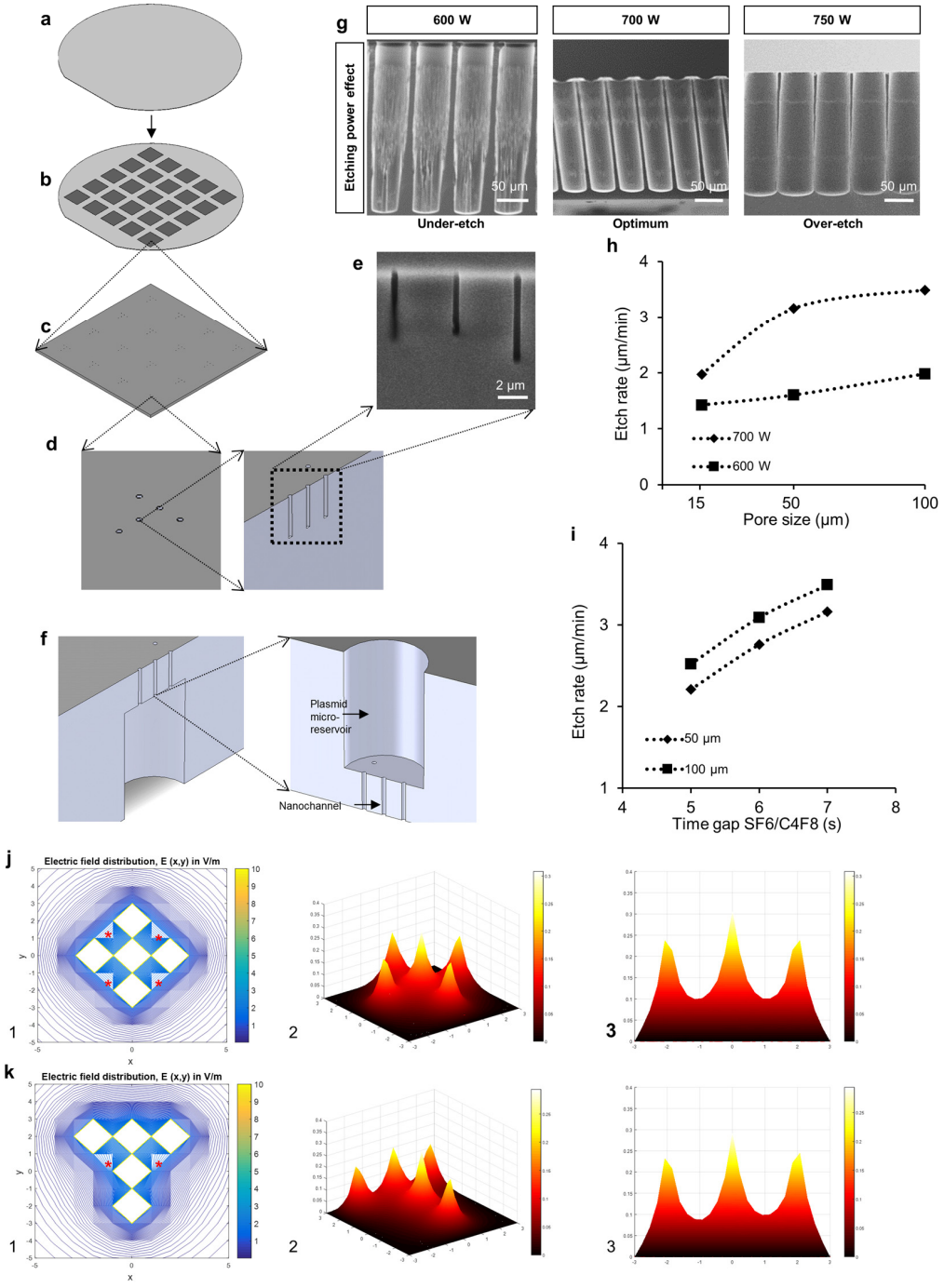

Supplementary Figure 1. TNT platform fabrication and nanochannel array simulation. (a) Double side polished silicon wafer. **(b-d)** Nanochannel patterning and DRIE. **(e)** Scanning electron microscopy (SEM) image of the etched nanochannels. **(f)** Back-side etching of microreservoirs.

(g) SEM micrographs and **(h, i)** plots showing etching profiles and etch rates, respectively, under different conditions. **(j, k)** Simulation results showing field distribution (**j1, k1**) and heat dissipation profiles (**j, k 2-3**) for asymmetric (*i.e.*, T-shape) nanochannel arrays vs. symmetric (*i.e.*, cross-shaped) arrays. Bulk electroporation (BEP) is the current gold standard for non-viral gene delivery *in vivo*. Gene uptake in BEP, however, is a highly stochastic process, which is not only influenced by non-uniform electric fields, but also downstream and/or more passive processes such as endocytosis and diffusion, respectively[1-3]. As such, simple approaches that facilitate more active and deterministic gene delivery *in vivo* are clearly needed. Here we implemented cleanroom-based technologies (i.e., projection lithography, contact photolithography, and deep reactive ion etching –DRIE-) (**Supplementary Fig. 1 a-i)**) to fabricate silicon-based TNT devices for active non-viral gene delivery to naturally- (e.g., skin) or surgically-accessible (e.g., skeletal muscle) tissue surfaces in a more deterministic manner. The TNT platforms consisted of a massively-parallel array of clustered nanochannels interconnected to microscale reservoirs that could hold the genetic cargo to be transduced into the tissues. Briefly, arrays of ~400-500 nm channels were first defined on the surface of a ~200 μm thick double-side polished silicon wafer using projection lithography and DRIE. Simulation studies suggest that such asymmetric T-shape array provides some inherent advantages in terms of electric field distribution and heat dissipation compared to a more symmetric nanopore distribution, with asymmetric clusters of nanochannels exhibiting less inactive zones (**Supplemental Fig. 1 j1, k1, red stars**), while at the same time reducing by 20-25% the peak and valley temperatures (**Supplemental Fig. 1 j2-3, k2-3**). This was then followed by contact lithography-based patterning and DRIE-mediated drilling of an array of microreservoirs juxtaposing the nanochannels. Finally, the platform surface was passivated with a thin insulating layer of silicon nitride.

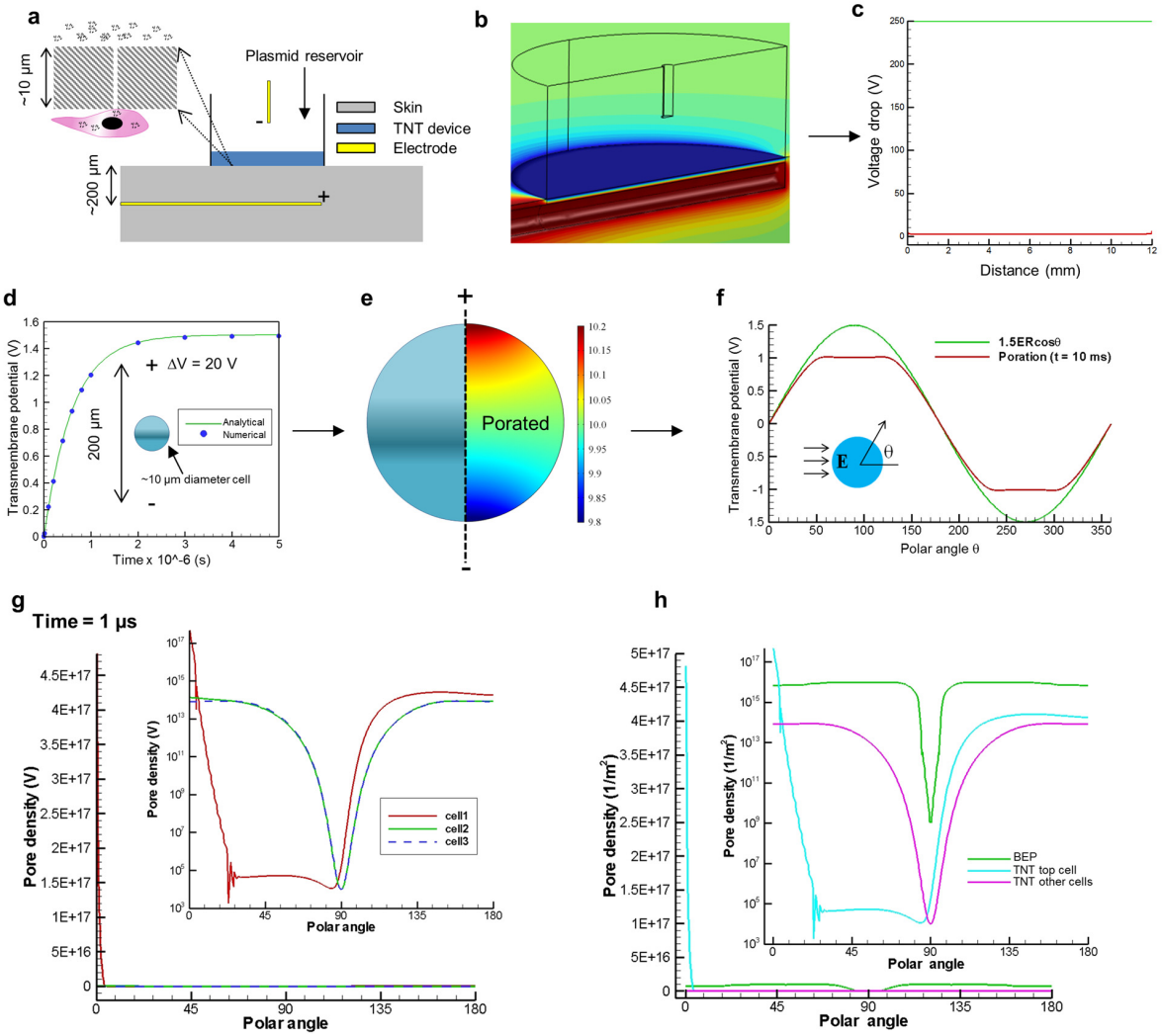

Supplementary Figure 2. Simulation results of *in vivo* nanochannel-based electroporation vs. bulk electroporation (BEP). (a) Schematic diagram illustrating the experimental set-up. **(b, c)** Simulated voltage distribution under a 250 V stimulation. **(d-f)** Simulation of transmembrane potential for single-cell bulk electroporation. **(g)** Poration profile for a cell in direct contact with the nanochannel (cell 1) compared to cells far away from the nanochannels (cell 2 and cell 3). **(h)** Poration profiles in TNT vs. BEP.

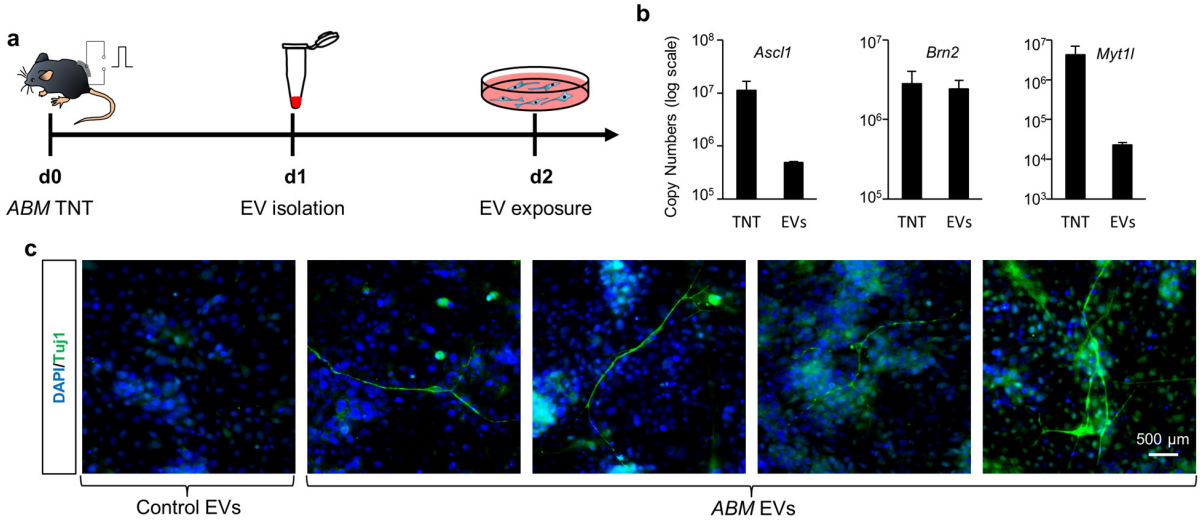

Supplementary Figure 3. EV-mediated cellular reprogramming. (a) Schematic diagram illustrating the experimental set-up. EVs are collected from *ABM* TNT-treated dorsal skin. **(b)** The *ABM* copy numbers from the EVs were quantified following a standard procedure[4, 5], and compared to the gene copy numbers delivered directly through TNT (from skin tissue collected immediately after transfection). Briefly, absolute qPCR quantification was used to assess the copy number of target genes within treated samples by relating the CT value to a standard curve. The standard curve was generated by utilizing a 10-fold-serial dilution series of each gene/plasmid. As expected, a sizable amount of *ABM* copies was detected in the EV isolate, which fell within the lower range of gene copy numbers delivered directly through TNT. **(c)** Additional experiments in which MEF cells were exposed to skin-derived EVs *in vitro* further indicate that such copy number magnitude is conducive to positive reprogramming outcomes, as evidenced by the presence of iNs when exposed to *ABM*-loaded EVs.

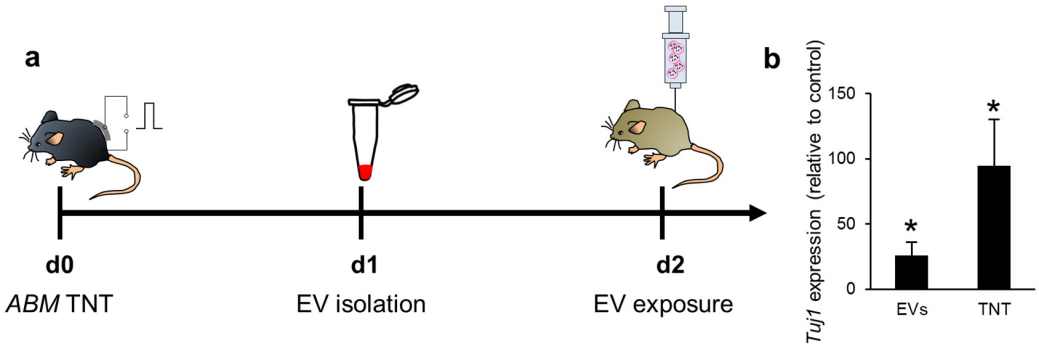

Supplementary Figure 4. Autologous *ABM*-loaded EVs isolated from TNT-treated dorsal skin exhibit neurotrophic-like characteristics when injected intradermally in naïve mice. (a) Schematic diagram illustrating the experimental set-up. EVs are collected from *ABM* TNT-treated dorsal skin and injected into naïve mice. **(b)** Tissue biopsies collected after 14 days show increase in *Tuj1* expression compared to control (untreated) mice. *ABM*-loaded EVs led to a ~26-fold increase in *Tuj1* expression. Comparatively, *ABM* TNT resulted in a ~94-fold increase in *Tuj1* expression, which reflects the net effect of direct reprogramming factor injection combined with EV-mediated propagation. Control specimens in this case are untreated skin biopsies. n= 3. * $p<0.05$ (Holm-Sidak method).

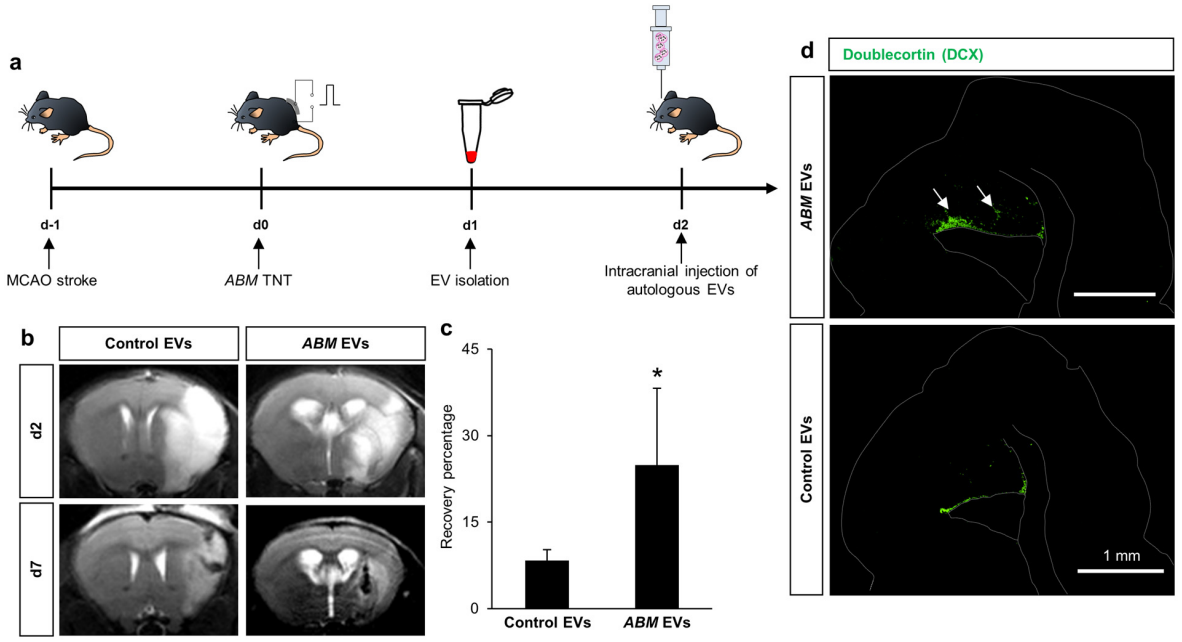

Supplementary Figure 5. Autologous *ABM*-loaded EVs isolated from TNT-treated dorsal skin exhibit neurotrophic-like characteristics in a MCAO stroke mouse (C57BL/6) model. (a) Schematic diagram illustrating the experimental set-up. MCAO stroke is first induced. This is then followed by *ABM* or control TNT treatment and EV isolation from dorsal skin prior to intracranial injection of EVs. **(b, c)** MRI imaging and quantification showing a significant reduction in the infarcted volume only 7 days after EV injection. **(d)** Immunofluorescence imaging 21 days after stroke induction showing DCX+ cells/processes projecting from the Subventricular (SVZ) zone towards the infarcted area (white arrows). DCX+ cells in control brains were found mostly lining the walls of the SVZ zone. Such preliminary findings suggest a potentially therapeutic effect for *in vivo*-derived EVs loaded with pro-neuronal factors. n= 4-5. * $p<0.05$ (Holm-Sidak method).

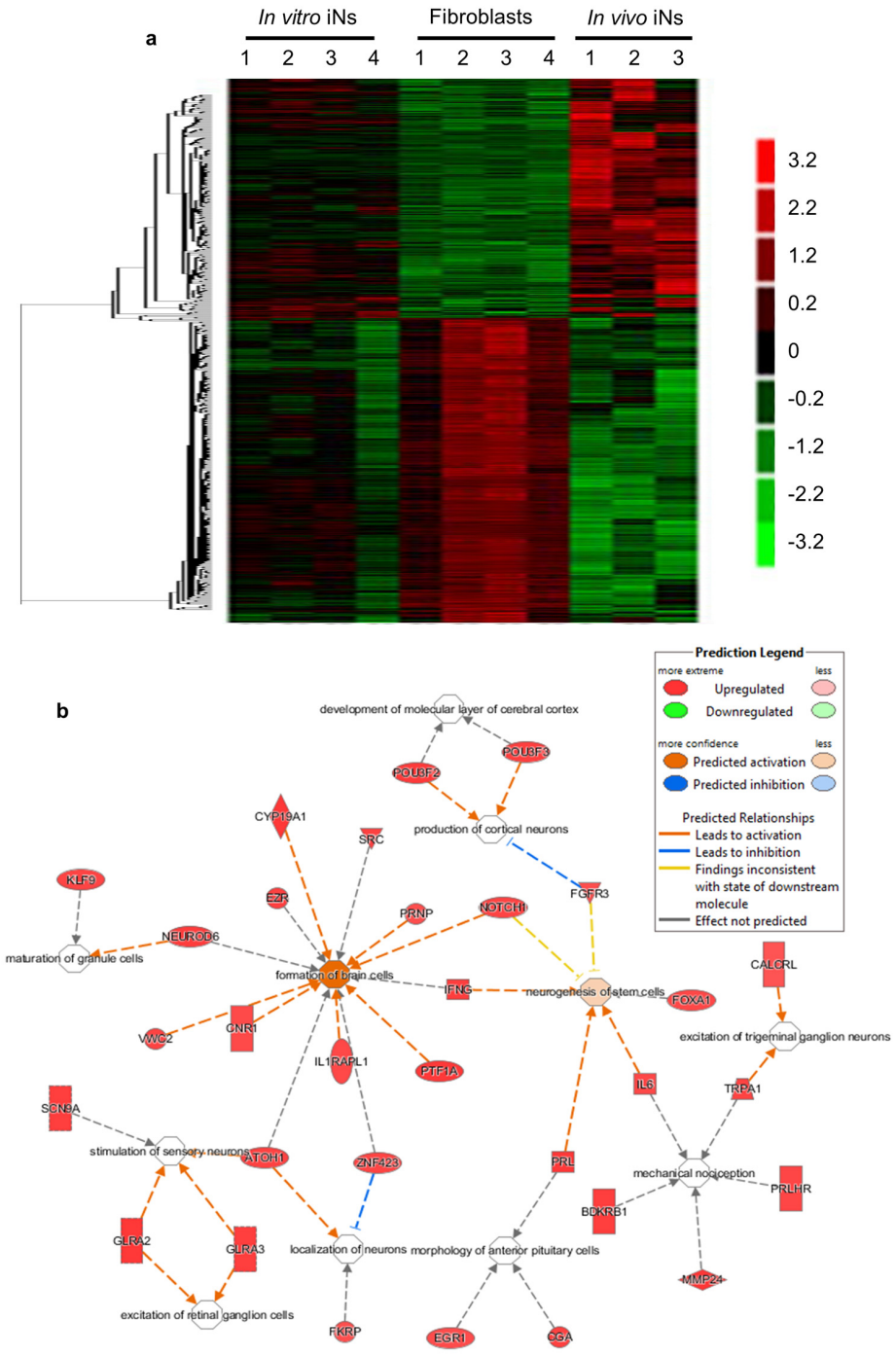

Supplementary Figure 6. Identification of gene expression profile homology between *in vitro* iNs versus *in vivo* iNs using GeneChip® microarray and IPA® analysis and clustering algorithms. iNs generated *in vitro* or laser-capture microdissected from *ABM*-transfected mouse

skin (*in vivo* iNs) were subjected to murine transcriptome array (MTA 1.0) analysis followed by data mining using clustering algorithms. *In vitro*-derived iN cultures were ontained via non-viral, electroporation-based delivery of *ABM*[6]. To identify homology in expression patterns between *in vitro* iNs versus *in vivo* iNs, the 26225 annotated probe-sets were clustered into 16 groups using k-means unsupervised learning algorithm. A cluster of *3503* probe-sets that showed expression pattern homology between *in vitro* iN versus *in vivo* iN groups, was subjected to IPA® analysis and hierarchical clustering. **(a)** The heat map represents genes (528) that were significantly different as compared to the unreprogrammed fibroblast group. **(b)** IPA® analysis showing induction of gene expressions. For further details for **(b)** see Tables 1 & 2 below. Microarray-IPA® analysis identified induction of genes implicated in brain tissue development, including a large cluster of genes associated with the olfactory response (among others) in both *in vitro*- and *in vivo*-derived iNs[7-10]. More robust induction was seen for the *in vivo* group.

Table 1. IPA analysis: functional annotation of the genes similar between *in vitro* iNs and *in vivo* iNs.

Functions Annotation	p-Value	# Molecules
Olfactory response	9.28E-96	315
Formation of brain cells	0.00539	13
Production of cortical neurons	0.00663	3
Development of molecular layer of cerebral cortex	0.00836	2
Excitation of retinal ganglion cells	0.00836	2
Excitation of trigeminal ganglion neurons	0.00836	2
Neurogenesis of stem cells	0.00945	6
Localization of neurons	0.0124	3
Abnormal morphology of vertebral body	0.0185	6
Stimulation of sensory neurons	0.019	4
Mechanical nociception	0.0198	5
Lack of cerebellum	0.0202	3
Maturation of granule cells	0.0236	2
Abnormal function of baroreceptor	0.0301	3
Morphology of anterior pituitary cells	0.0301	3

Table 2. Genes involved in IPA® analysis shown in Supplementary Fig. 5 b.

Symbol	Entrez Gene Name	Family	GenBank
ATOH1	Atonal bhlh transcription factor 1	Transcription regulator	NM_007500
BDKRB1	Bradykinin receptor B1	G-protein coupled receptor	NM_007539
CALCRL	Calcitonin receptor like receptor	G-protein coupled receptor	NM_018782
CGA	Glycoprotein hormones, alpha polypeptide	Other	NM_009889
CNR1	Cannabinoid receptor 1	G-protein coupled receptor	NM_007726
CYP19A1	Cytochrome P450 family 19 subfamily A member 1	Enzyme	NM_007810
EGR1	Early growth response 1	Transcription regulator	NM_007913
EZR	Ezrin	Other	NM_009510
FGFR3	Fibroblast growth factor receptor 3	Kinase	NM_001163215
FKRP	Fukutin related protein	Other	NM_173430
FOXA1	Forkhead box A1	Transcription regulator	NM_008259
GLRA2	Glycine receptor alpha 2	Ion channel	NM_183427
GLRA3	Glycine receptor alpha 3	Ion channel	NM_080438
IFNG	Interferon gamma	Cytokine	NM_008337
IL1RAPL1	Interleukin 1 receptor accessory protein like 1	Transmembrane receptor	NM_001160403
IL6	Interleukin 6	Cytokine	NM_031168
KLF9	Kruppel like factor 9	Transcription regulator	NM_010638
MMP24	Matrix metallopeptidase 24	Peptidase	NM_010808
NEUROD6	Neuronal differentiation 6	Transcription regulator	NM_009717
NOTCH1	Notch 1	Transcription regulator	NM_008714
POU3F2	POU class 3 homeobox 2	Transcription regulator	NM_008899
POU3F3	POU class 3 homeobox 3	Transcription regulator	NM_008900
PRL	Prolactin	Cytokine	NM_001163530
PRLHR	Prolactin releasing hormone receptor	G-protein coupled receptor	NM_201615
PRNP	Prion protein	Other	NM_011170
PTF1A	Pancreas specific transcription factor, 1a	Transcription regulator	NM_018809
SCN9A	Sodium voltage-gated channel alpha subunit 9	Ion channel	NM_018852
SRC	SRC proto-oncogene, non-receptor tyrosine kinase	Kinase	NM_009271
TRPA1	Transient receptor potential cation channel subfamily A member 1	Transporter	NM_177781
VWC2	von Willebrand factor C domain containing 2	Other	NM_177033
ZNF423	Zinc finger protein 423	Transcription regulator	NM_033327

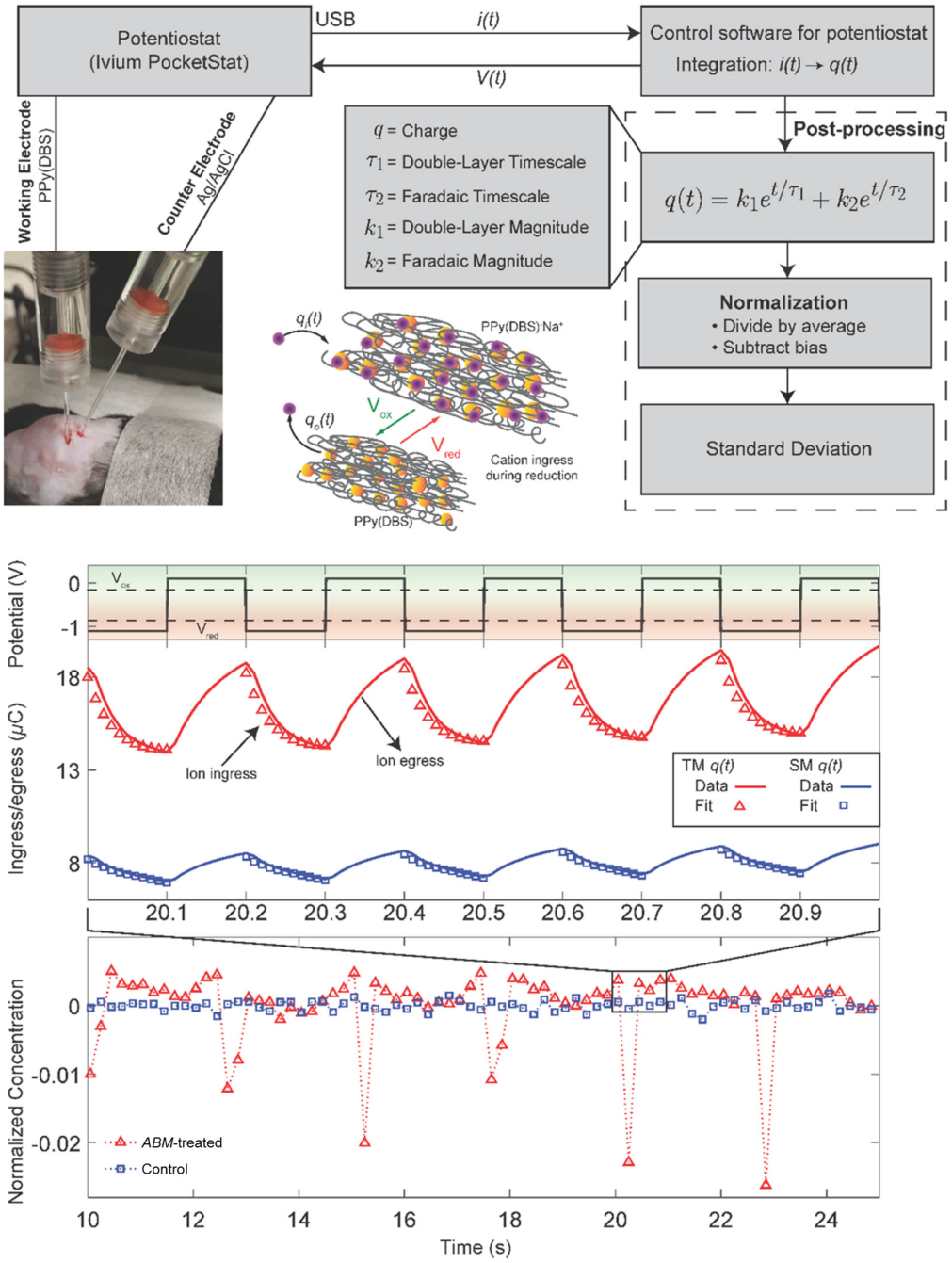

Supplementary Figure 7. *In situ* measurements of electrophysiological activity in the skin. **(a)** An information flow diagram detailing the *in vivo* action potential sensing process from experimental configuration (PPy(DBS) working electrode, Ag/AgCl counter electrode wires inserted with roughly 1-2 mm separation into the dermal layer and ionically connected with

physiological saline during 5 Hz oxidation-reduction events over the course of 20 seconds, to data collection (input electrical potential causing rapid oxidation-reduction events and measuring resultant current), post processing (calculating the number of ions participating in the transport phenomena in the vicinity of the working electrode and deriving time-dependent changes in concentration through fitting the charge equation for electrically conductive faradaic materials, normalizing the data set by dividing the entire time dependent response by its average to remove experimental bias, and calculating a standard deviation to quantify excitability of local cells), and interpretation (determining if the resultant deviations from the normalized plots are in excess to the background electrical noise to determine if the cells near the PPy(DBS) tip are excitable cells), **(b)** a conceptual schematic depicting ion transport in the near field of a conducting polymer and demonstrating the concentration dependence on the rate of ion transfer as well as a conceptual schematic demonstrating the difference between how excitable and non-excitable cells regulate their surrounding media, **(c)** a plot of the input potential (V) between the working and counter/reference electrodes over 1 second, resultant charge calculated (μC) from the measured current (μA) response during the same 1 second, a fit of the charge equation to determine the value of the concentration-dependent K_2 during reduction events, and a representative K_2 vs time plot for a representative *ABM*-treated (excitable) and control sample. The fully detailed process can be found below.

Experimental Methodology – Outline. We focused our efforts on detecting the inherent excitability of induced neurons *in vivo*, and we used the general principle of extracellular recording to achieve this goal. However, traditional electrophysiological techniques used for extracellular recordings were challenging to implement due to our need to dissect the tissue away from the mouse, identify the induced neurons morphologically, and then place an extracellular electrode in

close proximity to the cells of interest. To overcome aforementioned complexities of performing a patch-clamp technique or conventional electrophysiological measurement, chronoamperometric measurements of a conducting polymer electrode placed in the extracellular space were used to detect neuronal excitability. The transfer function for charge ingress and egress in to and out of the polymer is applied to measured data, and poles and residues corresponding to double layer and faradaic response of the conducting polymer are calculated. The residues calculated from transfer function analysis correspond to the changes in cation concentration proximate to the polymer as explained in Venugopal *et al*[11]. We demonstrate that by placing the conducting polymer electrode in the *ABM*-treated area of the mouse as shown in **Supplementary Figure 6**, temporal changes to the residue corresponding to faradic responses are observed, indicating neuronal excitability.

Physics of Operation for Redox-based Conducting Polymer Cation Sensors. Polypyrrole doped with dodecylbenzenesulfonate (PPy(DBS)) is a conducting polymer that exchanges cations with a local media at the onset of electrical potentials. The rate of cation ingress is a function of the applied electrical potential, polymer geometry, the current state of the polymer, and concentration of electrolyte[12]. This concentration dependence enables the creation of cation sensors which have been demonstrated to have a linear relationship with NaCl concentrations over the range of 5-100 mM[11]. Further, PPy(DBS) sensors are nontoxic and redox-mediator free systems capable of determining the local cation concentration of biological material without damaging or affecting their function[13]. Therefore, mesoscale PPy(DBS) sensors have been fabricated into probes capable of residing within the dermal layer to measure *in situ* cation concentration.

A single oxidation-reduction switch (redox event) of a PPy(DBS) membrane causes both faradaic and double-layer based ion transport. The time-dependent ion transport kinetics are

described by the equation below, where k_1 and τ_1 values correspond to the total number and rate of ions forming the electrical double layer and the k_2 and τ_2 values correspond to the total number and rate of ions intercalating into the polymer. Based on this, the effects of the double layer capacitor can be neglected leaving the k_2 value as the sensitive parameter to cation concentration[11].

$$q(t) = k_1 e^{\frac{t}{\tau_1}} + k_2 e^{\frac{t}{\tau_2}}$$

In order to capture time-dependent changes in cation concentration, multiple redox cycles of PPy(DBS) are required. The frequency of switching should be chosen based on an estimation of the rate of concentration change within the system of interest. In this instance, the rate of electrophysiological activity was unknown, so the redox frequency was chosen to be 5 Hz. At this frequency, the time for each reduction cycle is significantly lesser than the time required for the system to reach a steady state (2.5-10 seconds based on polymer thickness and electrolyte concentration)[14]. This causes the polymer to operate in constant flux between each redox state and creates a condition in which k_2 is varied due to the total number of ions that the polymer can accept within a 0.1 second window. The measured k_2 is therefore proportional to the local cation concentration. Monitoring changes in k_2 over time directly measures changes in cation concentration due to excitability of local cells.

Fabrication of PPy(DBS) Microelectrodes. Platinum wire (0.025 mm dia., 99.9% pure temper hard from Goodfellow, USA) was inserted through quartz capillaries (75x1 mm, Sutter Instruments) to form a 2 mm protrusion. The protrusion-end was sealed with epoxy, leaving a 1 mm exposed platinum wire as a working electrode (WE). Silver wire (0.5 mm dia., 99.9% pure from Sigma Aldrich) was similarly treated to form a reference electrode (RE) with a 1 mm protrusion. Prior to insertion, the silver wire was soaked for 20 minutes in sodium hypochlorite solution (10-15% chlorine) to form an Ag/AgCl layer. An electropolymerization solution (0.2 mM

pyrrole, 98% purity and 0.1 mM sodium dodecylbenzenesulfonate from Sigma Aldrich) was formed and allowed to settle for 30 minutes. The electropolymerization cell consisted of the Pt wire, the Ag/AgCl, and a platinum wire counter electrode (CE). A cyclic voltammetry experiment (CV) was performed to verify the electrochemical connectivity, pyrrole activity, and polymer growth region. A chronoamperometry experiment (CA) was subsequently performed with an applied 0.52 V potential (based on the CV) until 118.5 μC charge was deposited to create a PPy(DBS) membrane with a 0.15 $C.cm^{-2}$ charge density. The PPy(DBS) tips were then rinsed with DI water and dried under a nitrogen stream.

Equilibration and Calibration of PPy(DBS) Microelectrodes. After drying under a N_2 stream, the PPy(DBS) sensors were equilibrated in a stock solution similar to physiological conditions (125 mM NaCl from Sigma Aldrich in DI water). This was done by CV over 10 cycles to ensure a redundant current response over cycles and increase the sensitivity of the PPy(DBS) tips to cation ingress[15].

Protocol for Detection of Neuronal Excitability. Mice were categorized as either *ABM*, or control and sedated prior to measurement. Two 1 mm perforations were created in the dermal layer (3-5 mm apart). To ensure electrolytic conductivity throughout the epidermis, a physiological 0.9% NaCl solution was injected between the holes. The PPy(DBS) probe and Ag/AgCl probe were then inserted into the injection sites using nanopositioners (Sutter Instruments) such that 1 mm of each probe was exposed to the epidermal layer. A cyclic voltammogram was then recorded to ensure electrochemical connectivity and characterize the noise in the system. Subsequently, a series of chronoamperometric measurements was performed by switching between a reduction and oxidation potential every 0.1 seconds until 100 redox cycles were completed over the course of 20 seconds. The applied reduction and oxidation potential were selected based on the redox peaks

observed during the CV (0.2 V lesser than the reduction peak and 0.2 V greater than the oxidation peak). A 5 second equilibration (0 V applied) CA was performed before and after the redox switching. The CA process was repeated 5 to 10 times until the responses were similar between trials, indicating steady state behavior. There were multiple trials recorded at one insertion site, as well as multiple insertion sites. This was done to increase the chances of capturing neuronal cell activity, as the insertion sites were made arbitrarily.

Baseline Characterization of Sensor Response to Concentration Variation. To further understand the impact of environmental noise on the sensors, cyclic voltammometric and chronoamperometric measurements were performed (using the methods described above) using 0.9% NaCl solution in a 10 mL container. This experiment was used to establish a baseline metric wherein the inherent noise of the system was characterized. This was used to define the "activity" of *ABM* or control mice. According to this, a 3% +- deviation was considered to be evidence of "excitable" cells. To eliminate transience, the first 25 cycles of the measurement were ignored. Of the remaining 75 redox cycles, only the reduction cycles were considered, to capture the effect of ion ingress while ignoring ion egress. A two-term exponential function was fit to the data using the model described in the first section, and k_2 values were obtained. It was noticed that there was a time-dependent bias as well as a substantial offset between electrodes. Consequently, the k_2 values were normalized by dividing the k_2 values by their average, and subtracting a fifth-order polynomial fit. Using this method gave an objective basis for comparison, independent of electrode used.

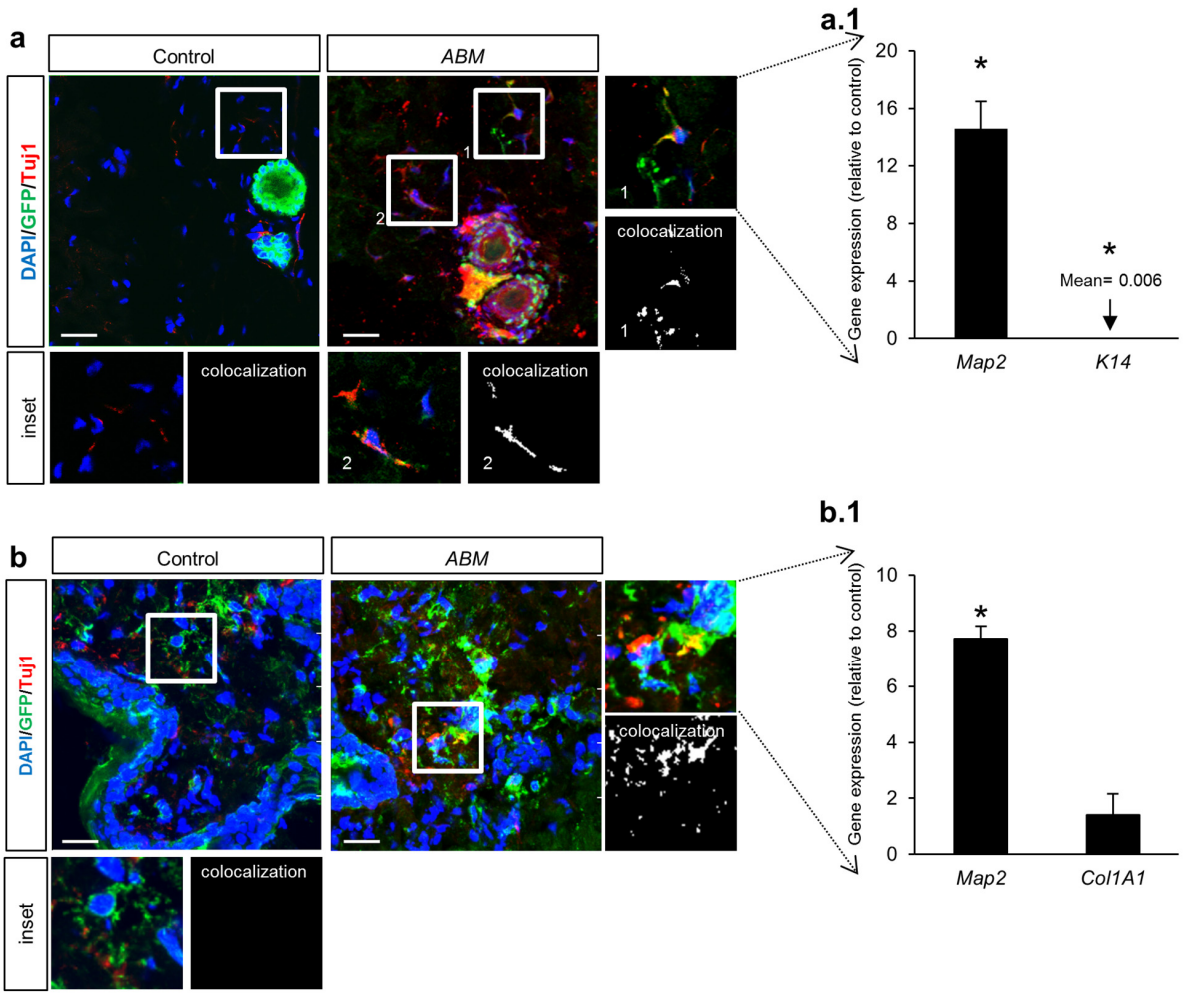

Supplementary Figure 8. iNs in the skin originate from epidermal and dermal sources. Fluorescence micrographs of *ABM*-treated skin sections from the **(a)** K14-Cre reporter mouse model and the **(b)** Col1A1-GFP mouse model showing skin cells of K14, or Col1A1 origin (green/GFP) also expressing the Tuj1 neuronal marker. The secondary antibody used for Tuj1 was CY5-tagged, and the emitting signal was pseudocolored red. The tdTomato background channel was excluded from the merged images. Scale= 20 µm. **(a.1, b.1)** Cellular elements that were immunoreactive for both the GFP tracer and Tuj1 were further analyzed by LCM/qRT-PCR. The results indicate that such double-positive elements had significantly high neuronal marker gene expression and moderate to markedly reduced skin cell marker gene expression. n= 3. * $p<0.05$

(Holm-Sidak method). Lineage tracing experiments with a K14-Cre reporter mouse model, where Keratin 14 positive (K14+) cells undergo cre-mediated recombination of the ROSA locus ultimately switching from tdTomato expression to eGFP, confirmed that the newly-induced neurons partly originated from K14+ skin cells. Experiments with a Col1A1-eGFP mouse model, where cells with an active Col1A1 promoter express eGFP, showed a number of Collagen/eGFP+ cells from the dermis in a transition phase to Tuj1+. Persistent Col1A1/GFP activity in these cells clearly reflects a gradual phenotypical shift between fibroblasts and induced neurons. LCM was used to capture and further characterize the gene expression profile of cellular elements from tissue sections of the transgenic mouse model that were both GFP+ and Tuj1+, which would correspond to cells that were of K14 origin but now express a neuronal marker, or cells that have an active collagen promoter (e.g., fibroblasts) transitioning to a neuronal fate. Our results indicated that such elements indeed exhibited increased expression of pro-neuronal markers, and reduced expression of the cell-of-origin marker (i.e., K14, Col1A1).

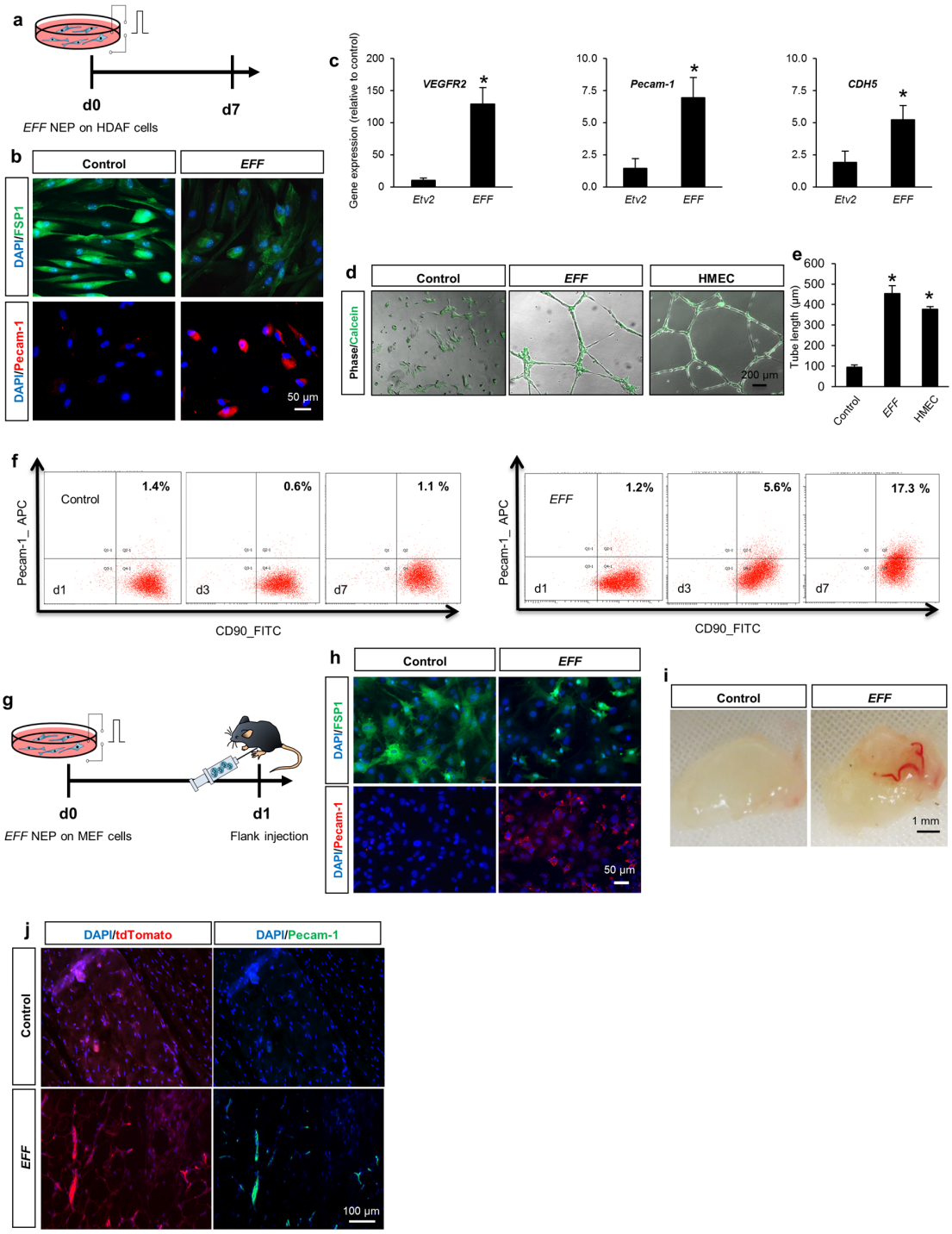

Supplementary Figure 9. The *EFF* gene cocktail drives faster and more efficient fibroblast reprogramming into an endothelial fate (iECs). (a) HDAF cells were non-virally transfected with *EFF*. **(b)** Fluorescence micrographs showing strong expression of the endothelial marker

Pecam-1 as well as reduced expression of the fibroblastic marker FSP (t= 7 days post transduction). **(c)** Gene expression analysis of endothelial markers for two different transduction conditions (*Etv2* alone vs. co-transfection of *EFF*). Results show a marked difference in gene expression, with *EFF* resulting in significantly stronger endothelial gene expression at day 7 post-transduction compared to *Etv2* alone. **(d, e)** Results from a tube formation assay showing that *EFF*-transduced cells were able to form blood vessel-like structures when cultured in matrigel comparable to endothelial cells (HMEC, positive control). Control HDAF cells, on the other hand, were not able to form tube-like structures when cultured in matrigel. **(f)** Flow cytometry-based analysis of endothelial and fibroblastic marker expression at days 1, 3 and 7 after *EFF* transfection. By days 3 and 7, approximately 6% and 17% of the population exhibited expression of Pecam-1, respectively, compared to control cells. Such dynamics agree with the timeline seen for increased perfusion following *EFF* TNT on dorsal skin (**Fig. 3**). Increased *in vivo* perfusion in response to *EFF* TNT, however, may not necessarily be entirely driven by reprogramming of stromal tissue into vascular tissue. Remodeling/sprouting of pre-existing vascular beds could be a contributing factor as well. **(g, h)** MEF cells non-virally transfected with *EFF* also show endothelial marker expression as early as 7 days post-transfection. **(i, j)** tdTomato-MEF cells non-virally transfected with *EFF* fomented blood vessel formation following flank injection in NSG mice. n=3-4. * $p<0.05$ (Holm-Sidak method).

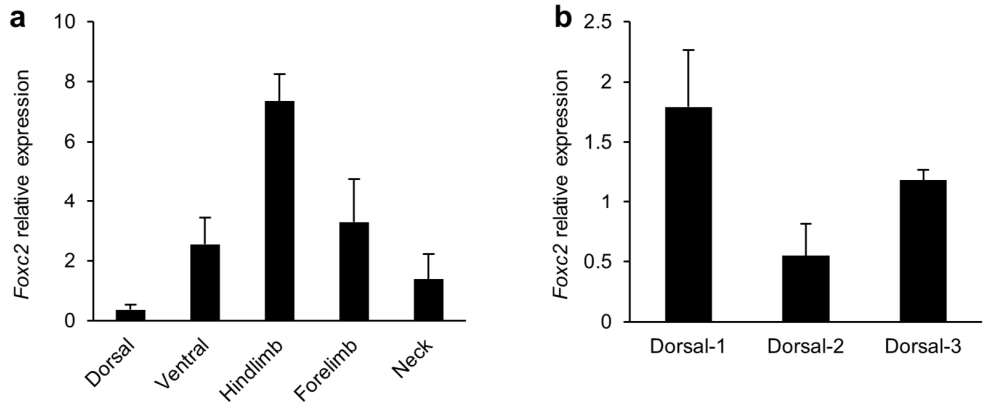

Supplementary Figure 10. Variations in endogenous *Foxc2* expression. Relative *Foxc2* expression in skin biopsied from **(a)** multiple locations or **(b)** different mice (same location). n=3.

Although recent *in vitro* studies by Morita and collaborators[16] reported that genomic integration of lentiviral *Etv2* vectors could induce direct endothelial reprogramming in cell lines with high levels of endogenous Foxc2, we found that ubiquitous *Foxc2* expression varies significantly *in vivo* (**Supplementary Fig. 6**), thus implying that in some cases low levels of endogenous Foxc2 expression may hamper successful endothelial induction via non-viral episomal expression of *Etv2* alone. As such, we proposed and tested a novel cocktail of transcription factors based on *Etv2*, *Foxc2*, and *Fli1* (*EFF*). Fli1 is a known intronic enhancer, and thus could have the ability to potentiate the reprogramming cocktail efficacy[17].

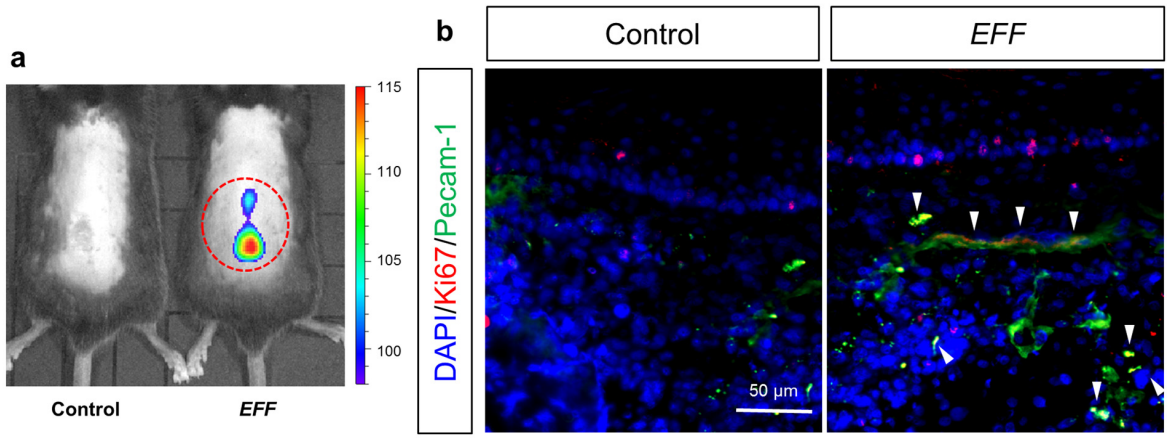

Supplementary Figure 11. *EFF*-treated skin shows signs of enhanced cell proliferation. (a) IVIS luminescence analysis in repTOP™ *mito*IRE mice confirms proliferative activity on dorsal skin of *EFF* TNT-treated mice (dotted red line). These mice express a luciferase reporter under the control of an artificial promoter derived from the Cyclin B2 gene, which is specifically induced during cellular proliferation[18]. **(b)** Immunofluorescence analysis of dorsal skin showing co-localization of proliferation markers (Ki67) with endothelial markers (Pecam-1).

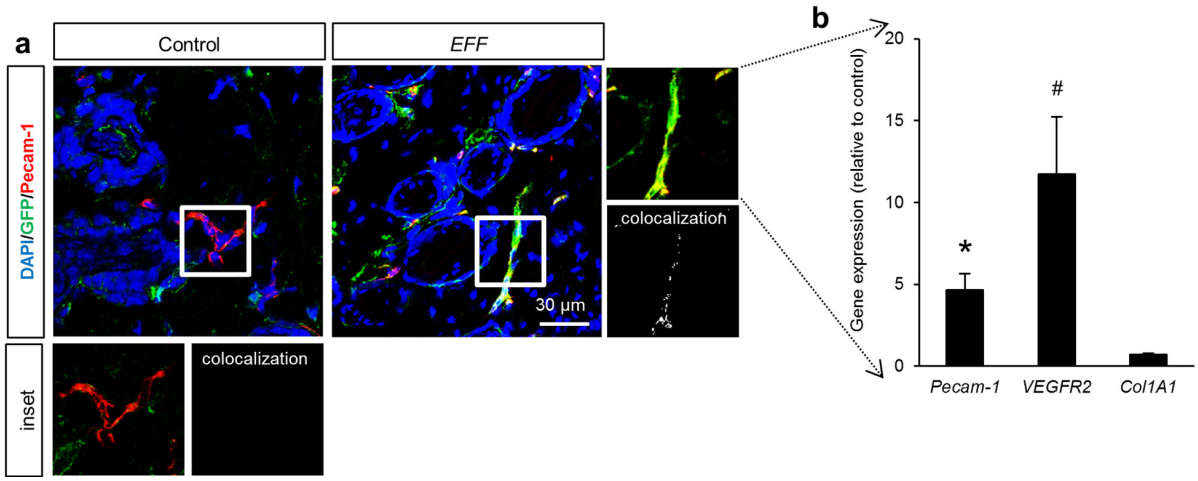

Supplementary Figure 12. iECs in the skin originate from Col1A1-expressing dermal sources. Fluorescence micrographs of *EFF* TNT-treated skin sections from the **(a)** Col1A1-GFP mouse models showing skin cells of Col1A1 origin (green) also expressing the Pecam1 endothelial marker, as they presumably transition from a fibroblast to an endothelial phenotype. **(b)** Cellular elements that were immunoreactive for both the GFP tracer and Pecam1 were further analyzed by LCM/qRT-PCR. The results indicate that such double-positive elements had significantly high endothelial marker gene expression. n=3. * $p<0.05$ (Holm-Sidak method), # $0.05<p<0.07$ (one-tailed t-test). Experiments with the K14-Cre reporter and Col1A1-eGFP mouse models confirmed that the reprogrammed cell population had for the most part a dermal origin. Unlike the induced neurons model, we were not able to find clear evidence of cells of K14 origin expressing endothelial markers.

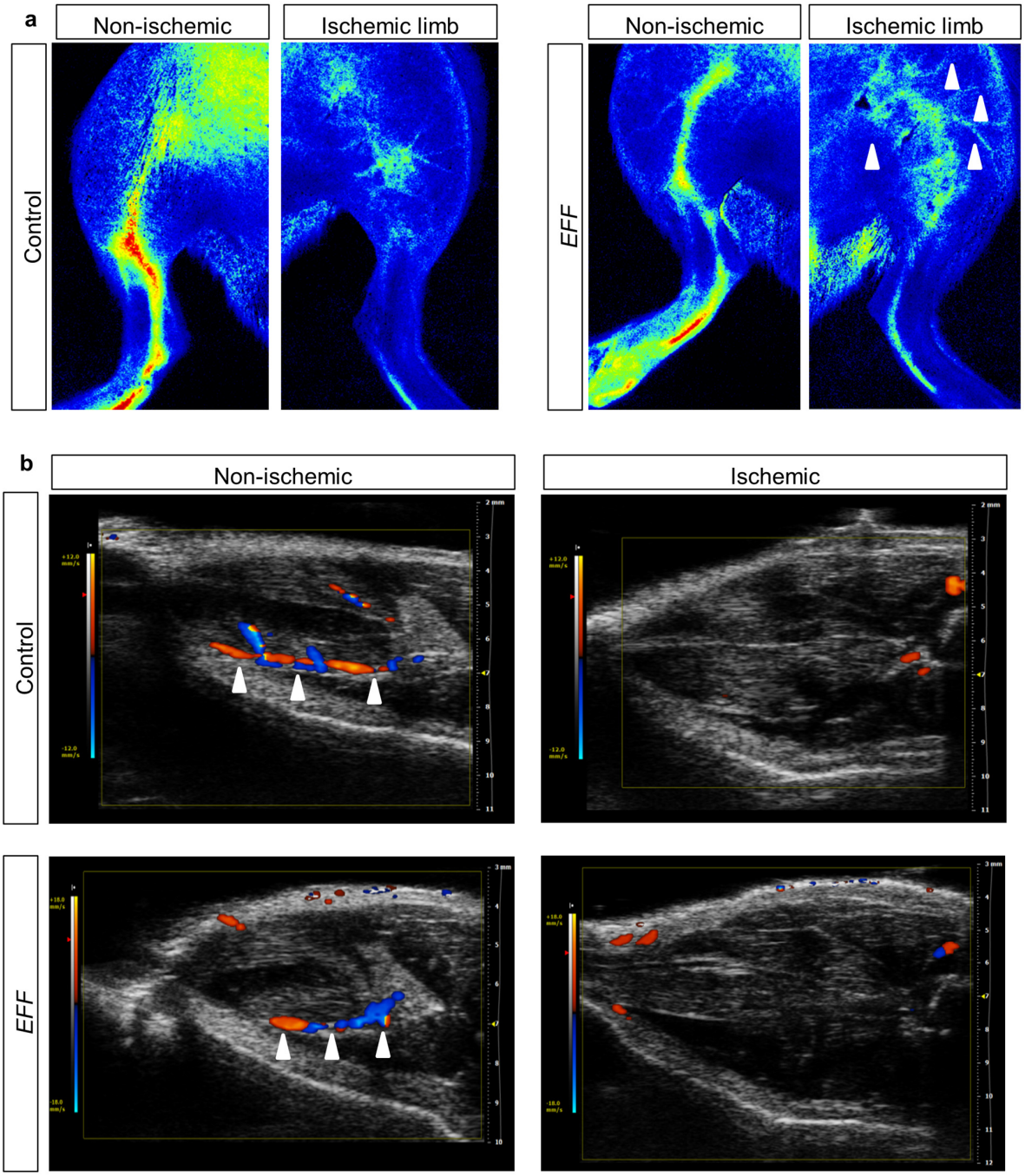

Supplementary Figure 13. HRLS and ultrasound imaging confirming transection of the femoral artery as well as increased incidence of collaterals in *EFF*-treated limbs. (a) HRLS imaging confirms the absence of a femoral artery in the ischemic limbs of both control and *EFF*-treated mice compared to their non-ischemic counterparts. Diffuse LS signal coming from the

EFF-treated limbs (white arrows) suggest the presence of smaller caliber collateral vessels that presumably mediate limb reperfusion. **(b)** Ultrasound imaging also confirmed the absence of a femoral artery in the ischemic limbs, thus further suggesting that limb reperfusion is likely modulated by the development of new/smaller collaterals and not the repair of the severed femoral artery.

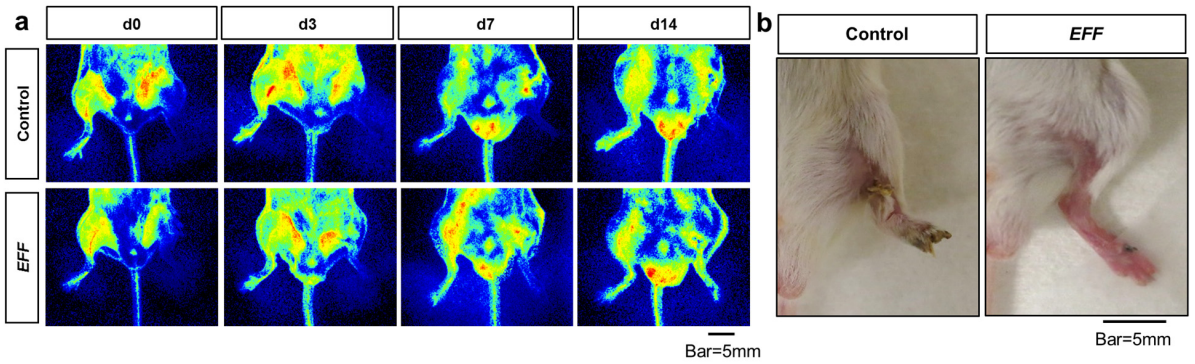

Supplementary Figure 14. *EFF* transfection helps to prevent necrosis in Balb/c hindlimb ischemia models. (a) Laser speckle imaging of the limbs showing successful reperfusion after *EFF* transfection. **(b)** Macroscopic changes to the ischemic limb with and without *EFF* treatment.

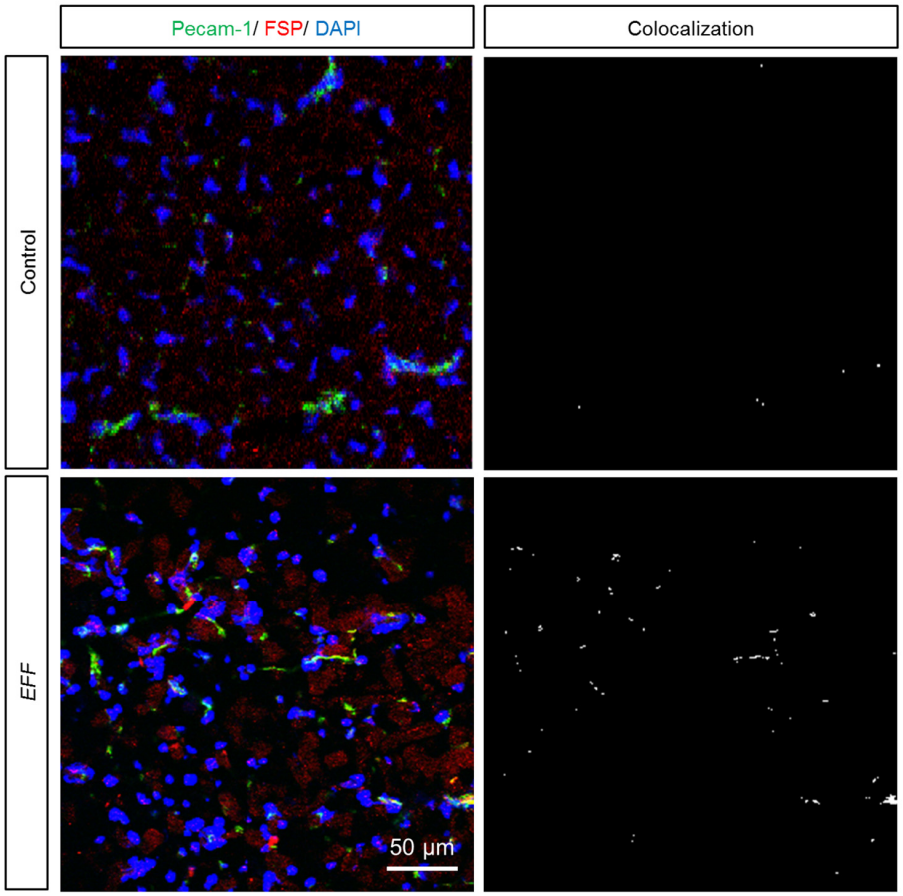

Supplementary Figure 15. Hindlimb ischemia experiments conducted using a Fsp1-Cre:R26R^{tdTomato} mouse model show that some of the Pecam-1+ cells in the gastrocnemius muscle also exhibited positive tdTomato reporter signal (colocalization shown in white), thus suggesting a possible fibroblastic origin (*e.g.,* skeletal muscle fibroblasts).

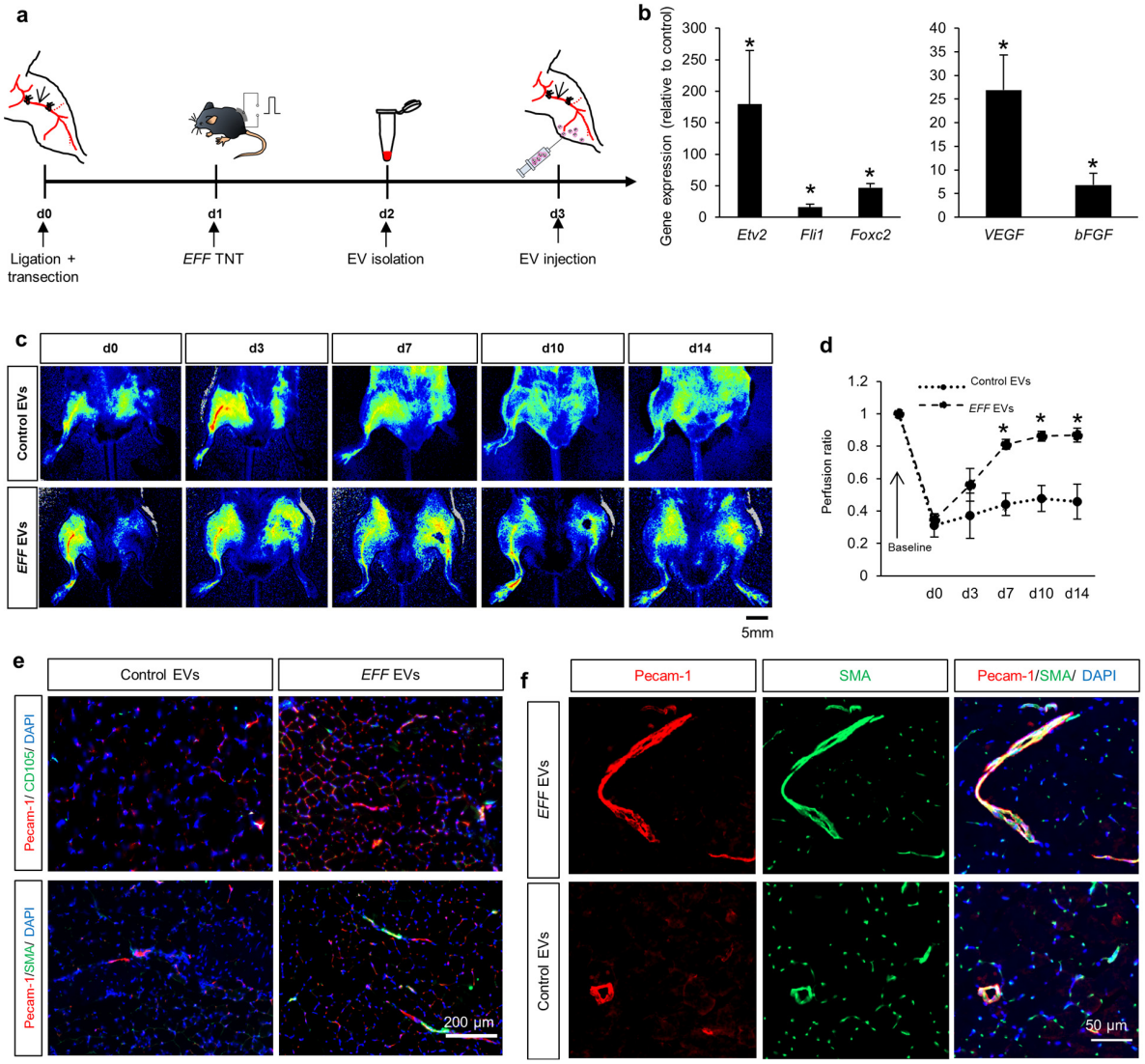

Supplementary Figure 16. EVs isolated from *EFF* TNT-treated dorsal skin help to mediate ischemic limb reperfusion. (a) Schematic diagram of injury/EV-mediated reperfusion. **(b)** qRT-PCR characterization of the EV content. These EVs were isolated from multicellular tissue structures, and thus such fold changes represent averaged values between EVs presumably carrying little to no *EFF* (and additional factors) cargo, and EVs with relatively large amounts of *EFF*. Additional experiments (**Supplementary Fig. 16**) confirmed that such EVs can reprogram remote naïve cells. **(c, d)** Laser speckle reperfusion analysis. **(e)** Immunofluorescence analysis of

the gastrocnemius muscle showing increased angiogenesis for the *EFF* EV-treated limb compared to control (*i.e.,* EVs derived from TNT-treated dorsal skin with a blank/mock solution). **(f)** High magnification micrographs showing co-expression of vascular markers following EV injection into the gastrocnemius. Such preliminary findings suggest a potentially therapeutic (proangiogenic) effect for *in vivo*-derived EVs loaded with pro-endothelial factors. n=3. * $p<0.05$ (Holm-Sidak method).

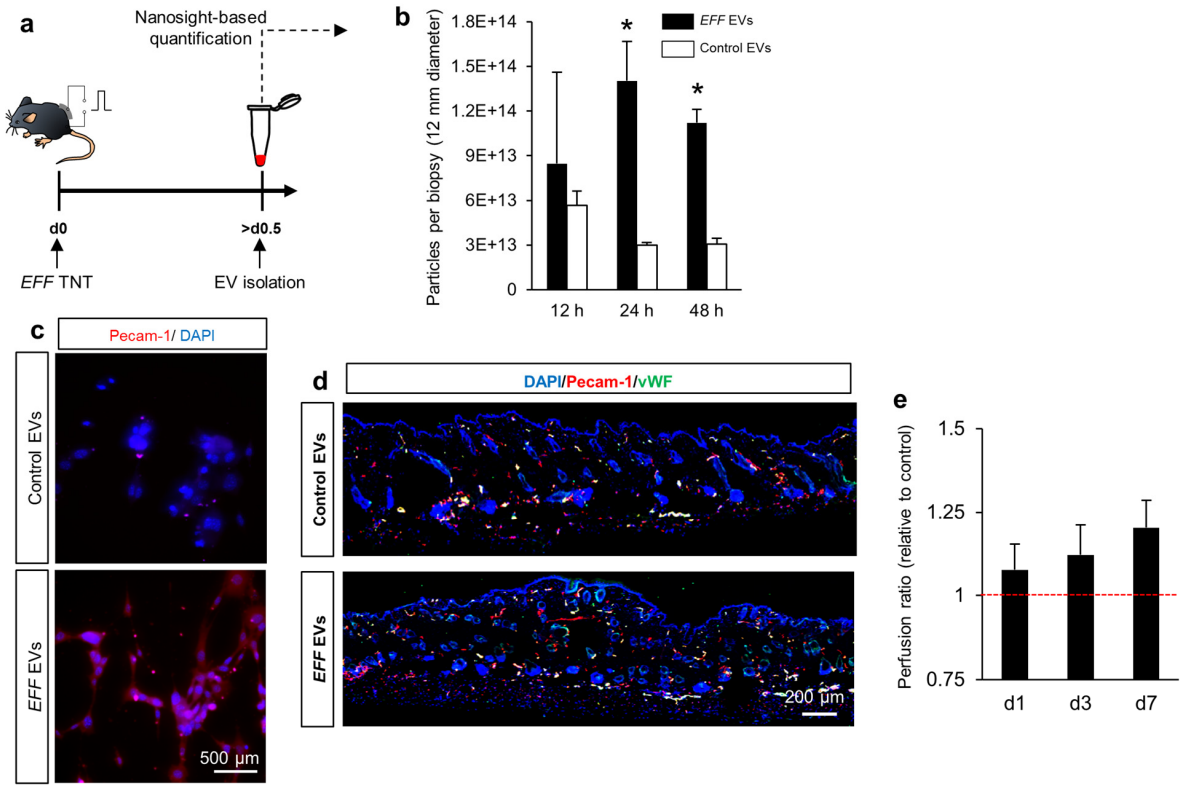

Supplementary Figure 17. *EFF*-laden EVs derived from *EFF*-transfected skin can modulate reprogramming in naïve cells. (a) EVs were isolated from TNT-treated (*EFF* vs. control) dorsal skin at different timepoints and analyzed via Nanosight. **(b)** *EFF* transfection led to increased release of EVs (>24 h) (n=3). **(c)** Exposing MEF cells to *EFF*-laden EVs resulted in the formation of discrete Pecam-1+ cellular pockets not seen in MEF cultures exposed to control EVs. Reprogramming efficacies, however, appear to be lower compared to direct nanochannel-based injection of *EFF* plasmids (**Supplementary Fig. 8**). This could be potentially due to multiple factors, including differences in the delivery mechanism (*e.g.,* direct electro-injection vs. endocytosis/fusion), and/or differences in local concentration between the *in vitro* and *in vivo* microenvironment. Additional experiments showed that **(d)** injecting *EFF*-laden EVs into uninjured tissue (*i.e.,* dorsal skin) led to a noticeable increase in cellular components expressing endothelial markers such as Pecam-1 and vWF. **(e)** Laser speckle analysis, however, showed only

a modest (~20%, $p>0.05$, ANOVA) increase in skin perfusion after day 3 compared to control EVs (red dashed line) (n=4). These findings suggest that the stimulus provided by *EFF*-laden EVs appears to be less likely to overcome the action of well-known angiostatic mechanisms responsible for modulating vascular homeostasis in healthy/uninjured tissues[19]. * $p<0.05$ (Holm-Sidak method).

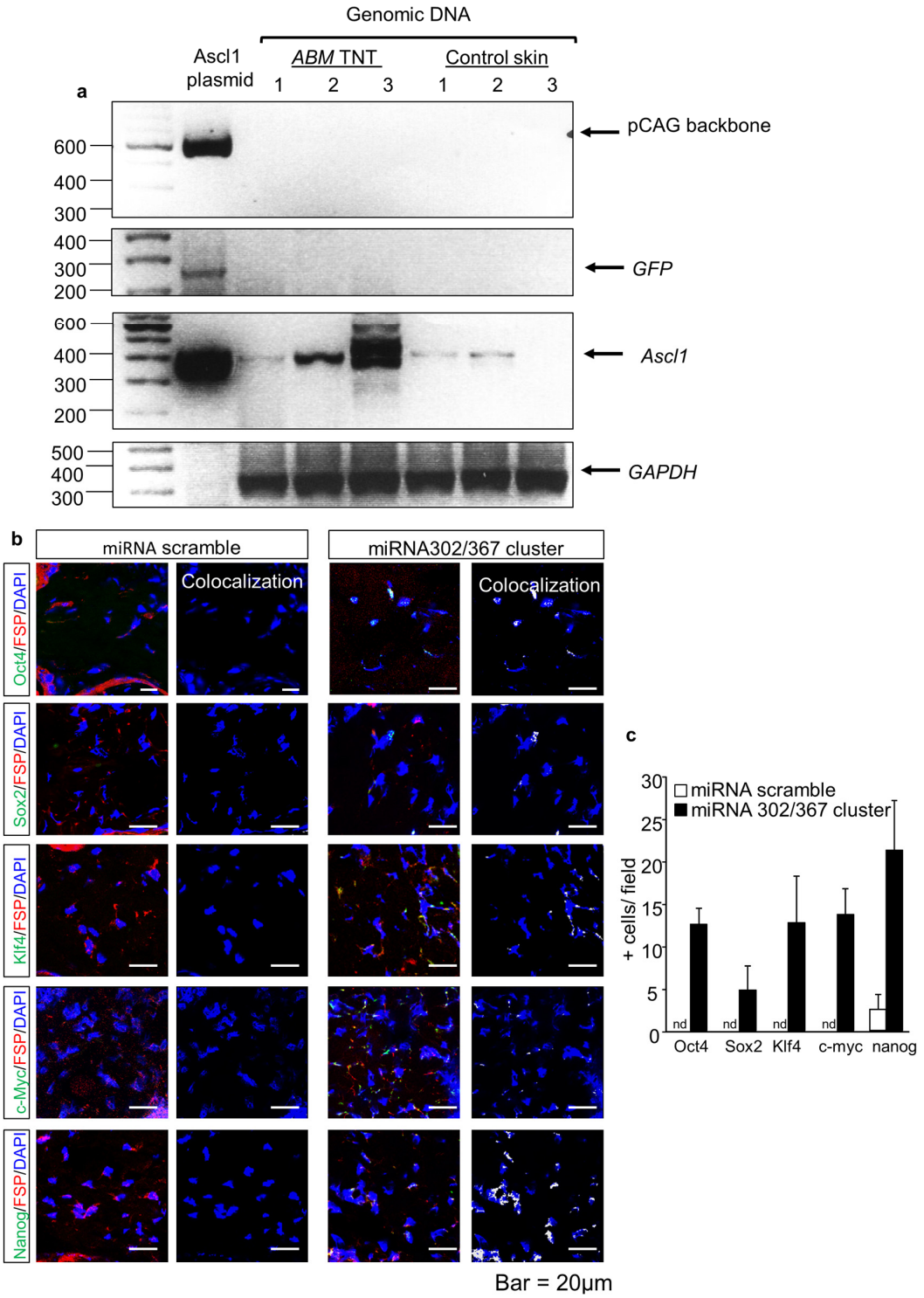

Supplementary Figure 18. TNT-based oligo RNA delivery and reprogramming. One of the limitations of plasmidic DNA-based reprogramming is the potential risk of insertional mutagenesis.

In order to determine if genomic integration occurred after TNT-mediated delivery of reprogramming gene plasmids, we conducted a PCR from genomic DNA isolated from TNT-treated skin, and screened for sequences matching the plasmid backbone and/or reporter genes. **(a)** Our results did not show any traces of the plasmid backbone or reporters in genomic DNA, thus suggesting insertion/integration was highly unlikely in this case. However, this does not preclude it from happening in the future, especially if the plasmid configuration is modified (*e.g.,* different backbones, linear vs. circular configurations, etc.). Taking this into consideration we proceeded to test whether the TNT platform could be used to reprogram skin tissue via RNA-based transfection. **(b, c)** TNT experiments with the microRNA302/367 cluster (*i.e.,* miRNA302a/b/c + miRNA367), which has been previously reported to induce pluripotency in somatic cells *in vitro*[20], showed that TNT-based delivery of such cocktail led to a marked induction of pluripotency markers in the skin as early as day 7. Induced pluripotency was not detected in skin tissue that was TNT-treated with scrambled miRNAs.

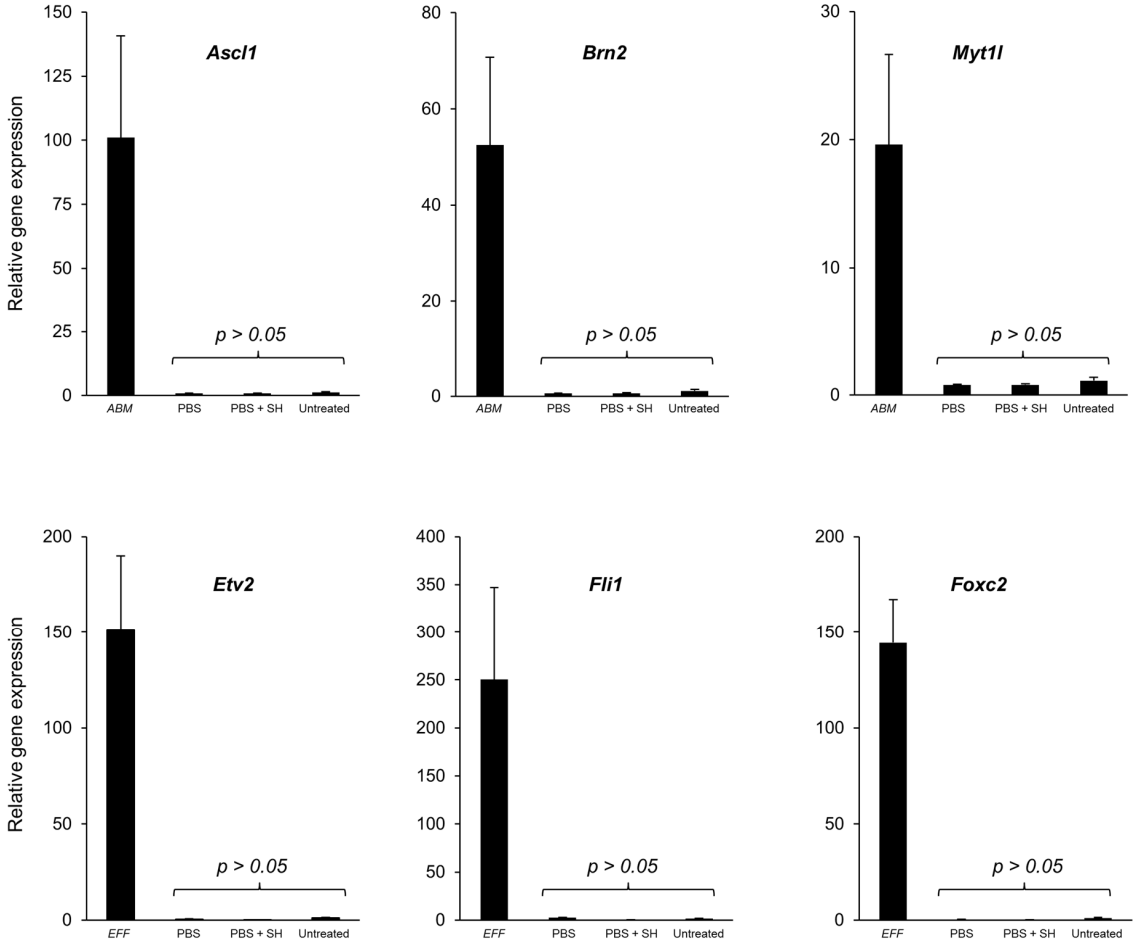

Supplementary Figure 19. Comparing different TNT controls. TNT was conducted on dorsal skin of C57BL/6 mice (n=3-5) with *ABM*/*EFF*, a blank solution of phosphate buffered saline (PBS), and PBS + sham/empty plasmids (PBS + SH). Untreated skin was used for comparison purposes. Gene expression analysis after 24 h shows no significant differences (ANOVA, Holm-Sidak method) between any of the control groups (PBS, PBS + SH, or untreated skin).

References

1. Geng T, Lu C. Microfluidic electroporation for cellular analysis and delivery. *Lab Chip* 2013, **13**(19)**:** 3803-3821.

2. Boukany PE, Morss A, Liao WC, Henslee B, Jung H, Zhang X, Yu B, Wang X, Wu Y, Li L, Gao K, Hu X, Zhao X, Hemminger O, Lu W, Lafyatis GP, Lee LJ. Nanochannel electroporation delivers precise amounts of biomolecules into living cells. *Nat Nanotechnol* 2011, **6**(11)**:** 747-754.

3. Gupta C, Liao WC, Gallego-Perez D, Castro CE, Lee LJ. DNA translocation through short nanofluidic channels under asymmetric pulsed electric field. *Biomicrofluidics* 2014, **8**(2)**:** 024114.

4. Whelan JA, Russell NB, Whelan MA. A method for the absolute quantification of cDNA using real-time PCR. *J Immunol Methods* 2003, **278**(1-2)**:** 261-269.

5. Lee C, Kim J, Shin SG, Hwang S. Absolute and relative QPCR quantification of plasmid copy number in Escherichia coli. *J Biotechnol* 2006, **123**(3)**:** 273-280.

6. Gallego-Perez D, Otero JJ, Czeisler C, Ma J, Ortiz C, Gygli P, Catacutan FP, Gokozan HN, Cowgill A, Sherwood T, Ghatak S, Malkoc V, Zhao X, Liao WC, Gnyawali S, Wang X, Adler AF, Leong K, Wulff B, Wilgus TA, Askwith C, Khanna S, Rink C, Sen CK, Lee LJ. Deterministic transfection drives efficient nonviral reprogramming and uncovers reprogramming barriers. *Nanomedicine* 2016, **12**(2)**:** 399-409.

7. Guillemot F, Lo LC, Johnson JE, Auerbach A, Anderson DJ, Joyner AL. Mammalian achaete-scute homolog 1 is required for the early development of olfactory and autonomic neurons. *Cell* 1993, **75**(3)**:** 463-476.

8. Treloar HB, Miller AM, Ray A, Greer CA. Development of the Olfactory System. In: Menini A (ed). *The Neurobiology of Olfaction*: Boca Raton (FL), 2010.

9. Jiang J, Chan YS, Loh YH, Cai J, Tong GQ, Lim CA, Robson P, Zhong S, Ng HH. A core Klf circuitry regulates self-renewal of embryonic stem cells. *Nat Cell Biol* 2008, **10**(3)**:** 353-360.

10. Louvi A, Artavanis-Tsakonas S. Notch signalling in vertebrate neural development. *Nat Rev Neurosci* 2006, **7**(2)**:** 93-102.

11. Venugopal V, Sundaresan VB. Polypyrrole-based amperometric cation sensor with tunable sensitivity. *J Intel Mat Syst Str* 2016, **27**(12)**:** 1702-1709.

12. Venugopal V, Zhang H, Northcutt R, Sundaresan VB. A thermodynamic chemomechanical constitutive model for conducting polymers. *Sensors and Actuators B: Chemical* 2014, **201**(0)**:** 293-299.

13. Venugopal V, Venkatesh V, Northcutt RG, Maddox J, Sundaresan VB. Nanoscale polypyrrole sensors for near-field electrochemical measurements. *Sensors and Actuators B: Chemical*.

14. Northcutt RG, Heinemann C, Sundaresan VB. Dynamic mechanoelectrochemistry of polypyrrole membranes via shear-force tracking. *Physical Chemistry Chemical Physics* 2016, **18**(26)**:** 17366-17372.

15. Venugopal V. Kinetics of Ion Transport in Conducting Polymers. The Ohio State University, 2016.

16. Morita R, Suzuki M, Kasahara H, Shimizu N, Shichita T, Sekiya T, Kimura A, Sasaki K, Yasukawa H, Yoshimura A. ETS transcription factor ETV2 directly converts human fibroblasts into functional endothelial cells. *Proc Natl Acad Sci U S A* 2015, **112**(1)**:** 160-165.

17. De Val S, Black BL. Transcriptional control of endothelial cell development. *Dev Cell* 2009, **16**(2)**:** 180-195.

18. Ghatak S, Li J, Chan YC, Gnyawali SC, Steen E, Yung BC, Khanna S, Roy S, Lee RJ, Sen CK. AntihypoxamiR functionalized gramicidin lipid nanoparticles rescue against ischemic memory improving cutaneous wound healing. *Nanomedicine* 2016, **12**(7)**:** 1827-1831.

19. Sen CK, Gordillo GM, Khanna S, Roy S. Micromanaging vascular biology: tiny microRNAs play big band. *J Vasc Res* 2009, **46**(6)**:** 527-540.

20. Anokye-Danso F, Trivedi CM, Juhr D, Gupta M, Cui Z, Tian Y, Zhang Y, Yang W, Gruber PJ, Epstein JA, Morrisey EE. Highly efficient miRNA-mediated reprogramming of mouse and human somatic cells to pluripotency. *Cell Stem Cell* 2011, **8**(4)**:** 376-388.

Supplementary Table 1. DNA Plasmids

Construct Name	Gene insert	Plasmid Backbone	Plasmid Source
Brn2	Brn2	pCAGGs	Constructed by ABM
Myt1l	Myt1l	pCAGGs	Constructed by ABM
Ascl1	Ascl1	pCAGGs	Constructed by ABM
pIRES-ER71(HA)$_3$	Etsvp71 (ER71)	pIRES-hrGFP-2a	Donated by Dr. Anwarul Ferdous, Department of Internal Medicine. UT Southwestern
pAd –HA-Fli1-IRES-hrGFP	HA-Fli1	pAd–IRES-GFP	Donated by Dr. Anwarul Ferdous, Department of Internal Medicine. UT Southwestern
mFoxc2	mFoxc2	pCDNA3.0	Donated by Dr. Tsutomu Kume, Department of Medicine-Cardiology and Pharmacology Northwestern University-FCVRI, Chicago
pCAGEN	NA (empty)	pCAGGs	pCAGEN was a gift from Connie Cepko (Addgene plasmid # 11160)[1]
Vitality IRES-hrGFP II	NA (empty)	pIRES-hrGFP II	Agilent Technologies
pcDNA™3.1	NA (empty)	pcDNA3.1	Invitrogen

Supplementary Table 2. List of primers

Primer/probe Name	Primer Sequence	Application
Ascl1_q_F	5'-CGACGAGGGATCCTACGAC-3'	Quantitative PCR
Ascl1_q_R	5'-CTTCCTCTGCCCTCGAAC-3'	Quantitative PCR
Brn2_q_F	5'-GGTGGAGTTCAAGTCCATCTAC-3'	Quantitative PCR
Brn2_q_R	5'-TGGCGTCCACGTAGTAGTAG-3'	Quantitative PCR
Myt1L_q_F	5'-ATACAAGAGCTGTTCAGCTGTC-3'	Quantitative PCR

Myt1L_q_R	5'-GTCGTGCATATTTGCCACTG-3'	Quantitative PCR
Etv2_F	5'-CGCGAGTTCCAGCTGTGCGA-3'	Quantitative PCR
Etv2_R	5'-GGCGAGGACAGGCACACGTC-3'	Quantitative PCR
Fli1_F	5'-GGGCTGGGCTGCAGACTTGG-3'	Quantitative PCR
Fli1_R	5'-GGGGCTGCCCGTAGTCAGGA-3'	Quantitative PCR
Foxc2_F	5'-TACGCGCCCTACCACCACCA-3'	Quantitative PCR
Foxc2_R	5'-GCCCTGCTTGTTCTCGCGGT-3'	Quantitative PCR
PECAM1_F	5'-GGACCAGTCCCCGAAGCAGC-3'	Quantitative PCR
PECAM1_R	5'-AGTGGAGCAGCTGGCCTGGA-3'	Quantitative PCR
VEGFR2_F	5'-AGCGCTGTGAACGCTTGCCT-3'	Quantitative PCR
VEGFR2_R	5'-CATGAGAGGCCCTCCCGGCT-3'	Quantitative PCR
EGFP-N	5'-CCGTCCAGCTCGACCAG-3'	Quantitative PCR
EGFP-C	5'-GATCACATGGTCCTGCTG-3'	Quantitative PCR
Cdh5_F	5'-GTGCAACGAGCAGGGCGAGT-3'	Quantitative PCR
Cdh5_R	5'-GGAGCCACCGCGCACAGAAT-3'	Quantitative PCR
m-K14 _F	5'-GCTGGTGCAGAGCGGCAAGA-3'	Quantitative PCR
m-K14_R	5'-AGACGGCGGTAGGTGGCGAT-3'	Quantitative PCR
m-Tuj1_F	5'-TACACGGGCGAGGGCATGGA-3'	Quantitative PCR
m-Tuj1_R	5'-TCACTTGGGCCCCTGGGCTT-3'	Quantitative PCR
m-Col1A1_F	5'-GTGTGATGGGATTCCCTGGACCTA-3'	Quantitative PCR
m-Col1A1_R	5'-CCTGAGCTCCAGCTTCTCCATCTT-3'	Quantitative PCR
m-MAP2_F	5'-AGGCCAGGTGGTGGACGTGT-3'	Quantitative PCR
m-MAP2_R	5'-CACGCTGGACCTGCTTGGGG-3'	Quantitative PCR
m-GAPDH_F	5'- ATGACCACAGTCCATGCCATCACT-3'	Quantitative PCR

m-GAPDH_R	5'- TGTTGAAGTCGCAGGAGACAACCT-3'	Quantitative PCR
p-CAGG_F	5'- TATGCTGGCTGCCATGAACA-3'	Semi-quantitative PCR
p-CAGG_R	5'- CTGGAATAGCTCAGAGGCCG-3'	Semi-quantitative PCR
Ascl1_F	5'-TCGTCCTCTCCGGAACTGAT-3'	Semi-quantitative PCR
Ascl1_R	5'-GTCCAGCAGCTCTTGTTCCT-3'	Semi-quantitative PCR
GFP_F	5'-CTGGTCGAGCTGGACGGCGACG-3'	Semi-quantitative PCR
GFP_R	5'-TGGTGCGCTCCTGGACGTAG-3'	Semi-quantitative PCR

Supplementary Table 3. Primary antibodies

Antibody Name	Company (catalogue #)	Dilution
Purified Rat Anti Mouse CD31	BD Pharmingen (550274)	1:400
Anti-S100A4 antibody	Abcam (ab27957)	1:200
Anti-Von Willebrand Factor antibody	Abcam (ab6994)	1:200
Anti-CD105 antibody	Abcam (ab107595)	1:400
Anti-Keratin 14	Covance (PRB-155P-100)	1:400
Anti-GFP	Abcam (ab32146)	1:500
Anti-Tuj1	Covance (MMS-435P)	1:500
Anti-Doublecortin	EMD Millipore (AB2253)	1:500
Anti-Ki67	Biolegend (652402)	1:400
Anti-Oct4	Abcam (ab19857)	1:200
Anti-Sox2	Abcam (ab97959)	1:200
Anti-Klf4	Abcam (ab72543)	1:200
Anti-c-Myc	Abcam (ab32072)	1:200
Anti-Nanog	Abcam (ab80892)	1:200

Supplementary Table 4. miRNA mimics

miRNA	Company	catalogue #
miRIDIAN microRNA Mouse mmu-miR-302a-3p mimic	Dharmacon	C-310483-05-0005
miRIDIAN microRNA Mouse mmu-miR-302b-3p mimic	Dharmacon	C-310669-05-0005
miRIDIAN microRNA Mouse mmu-miR-302c-3p mimic	Dharmacon	C-310671-05-0005
miRIDIAN microRNA Mouse mmu-miR-302d-3p mimic	Dharmacon	C-310672-05-0005
miRIDIAN microRNA Mouse mmu-miR-367 mimic	Dharmacon	C-310658-05-0005
miRIDIAN microRNA Mimic Negative Control #1	Dharmacon	CN-001000-01-05

References

1. Matsuda T, Cepko CL. Electroporation and RNA interference in the rodent retina in vivo and in vitro. *Proc Natl Acad Sci U S A* 2004, **101**(1)**:** 16-22.